Integrated photon-pair source with monolithic piezoelectric frequency tunability

T. Brydges,[1,*] A. S. Raja,[2] A. Gelmini,[1] G. Lihachev,[2] A. Petitjean,[1,†] A. Siddharth,[2] H. Tian,[3] R. N. Wang,[2] S. A. Bhave,[3] H. Zbinden,[1] T. J. Kippenberg,[2] and R. Thew[1]

[1]*Department of Applied Physics, University of Geneva, Geneva 1205, Switzerland*

[2]*Laboratory of Photonics and Quantum Measurements, École Polytechnique Fédérale de Lausanne (EPFL), Lausanne 1015, Switzerland*

[3]*OxideMEMS Lab, Purdue University, West Lafayette, Indiana 47907, USA*

(Received 16 January 2023; accepted 6 April 2023; published 3 May 2023)

This work demonstrates the capabilities of an entangled photon-pair source at telecom wavelengths, based on a photonic integrated Si_3N_4 microresonator with monolithically integrated piezoelectric frequency tuning. Previously, frequency tuning of photon pairs generated by microresonators has only been demonstrated using thermal control, however these have limited actuation bandwidth and are not compatible with cryogenic environments. Here, the frequency-tunable photon-pair generation capabilities of a Si_3N_4 microresonator with a monolithically integrated aluminium nitride layer are shown. Fast-frequency locking of the microresonator to an external laser is demonstrated, with a resulting locking bandwidth orders of magnitude larger than reported previously using thermal locking. These abilities will have direct application in future schemes which interface such sources with quantum memories based on, e.g., trapped-ion or rare-earth-ion schemes.

DOI: 10.1103/PhysRevA.107.052602

I. INTRODUCTION

Quantum photonic sources and interfaces are predicted to be a crucial component of future quantum networks, enabling the transfer of information with unprecedented security compared to current classical protocols [1–4]. In addition, the rapid development of quantum sensing, computation, and simulation technologies could eventually exploit reliable and robust quantum networks that distribute quantum information and entanglement as a resource. Such a network should also allow interfacing between the different technologies and platforms which may be used for these systems, such as photons [5,6], rare-earth ions [7–9], trapped ions [10–12], and nitrogen-vacancy centers [13,14].

Integrated photonics is a promising solution to this problem. It allows large numbers of components to be packaged together in a compact and stable manner [15], analogous to the packaging of electrical components in classical computers. Photonic integrated microresonators, in particular, have shown increasing potential for a wide range of applications over the past few years, including in coherent optical communication [16], frequency conversion [17], and chip-scale frequency comb sources [18]. As photon sources, microresonators have already demonstrated excellent performance [19–29]. They are compact, highly stable, and their heralding efficiencies have been shown to be comparable to some bulk optic, narrow-band cavity sources [28,30]—a crucial characteristic for scaling quantum communication to larger numbers of photons [31–33]. Silicon nitride (Si_3N_4) is an attractive platform for this technology, with low linear loss [34,35], negligible two-photon absorption in the telecom band [36], and a wide transparency range, from visible to midinfrared wavelengths [37]. The latter is especially advantageous with regards to interfacing between different quantum technology platforms, as some platforms are not at telecom wavelengths [7–9]. Moreover, key components such as narrow-linewidth lasers [38], amplifiers [39], and filters [40] can be fully integrated on a single chip, leading to mass manufacturable miniaturized quantum systems.

Integrated photonic Si_3N_4 microresonators have already shown they are well suited to the production of narrow-band photons at telecom wavelengths. More specifically, they have demonstrated bandwidths compatible with some rare-earth-ion quantum memories [24,28], which are a cornerstone of many quantum repeater architectures [3,30]. However, interfacing a photon source with a quantum memory for such a quantum-repeater-like architecture places very strict requirements on both the characteristics of the photons and the stability of the source itself. Of most relevance for this work is the ability for fast frequency tuning in order to achieve precise and stable frequency locking to the quantum memory. Typically, the ability to tune the resonance frequency of an integrated microresonator cavity (and by extension, the frequency of the generated photons) has only been possible by tuning the temperature of the device [19,20,23,24,27,28]. Temperature tuning is not ideal as it is relatively slow in comparison to electronic switching, with maximum actuation bandwidths on the order of 10 kHz [41,42], and impractical if the chip is to be used in cryogenic environments. In addition, temperature tuning is often monodirectional (i.e., active heating but passive cooling) [43].

In contrast, integrated piezoelectric controllers have the potential to provide fast frequency tuning, which is both

*tiffany.brydges@unige.ch

†Current address: Université Côte d'Azur, Institut de Physique de Nice, Nice, France.

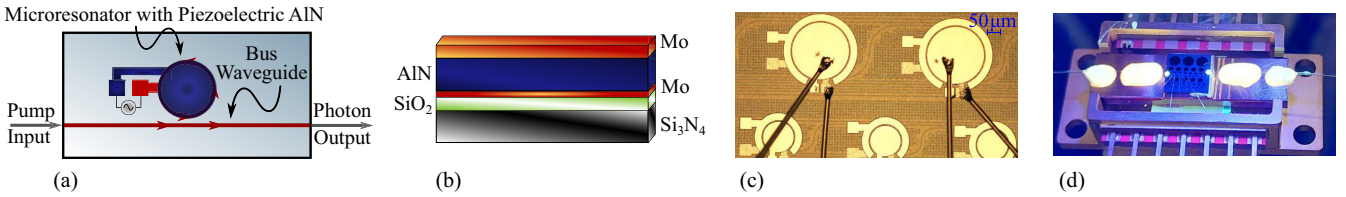

FIG. 1. (a) Schematic of the electrically tunable microresonator. A monolithically integrated layer of AlN (dark blue) is placed on top of the existing Si_3N_4 structures. A voltage source is connected to the AlN layer in order to provide piezoelectric frequency tuning. (b) Illustration of chip composition. The Si_3N_4 waveguide (black) is topped with a layer of silica cladding (green) to preserve the low propagation losses through the waveguide. A layer of molybdenum (red) acts as the bottom electrode, the AlN (dark blue) is the main piezoelectric material, with a final layer of molybdenum acting as the top electrode. See Ref. [44] for a detailed description of the chip design and fabrication process. (c) Microscope image of the electrically wire bonded AlN actuator on top of the Si_3N_4 microresonator. (d) Photograph of the optically and electrically packaged chip.

bidirectional as well as compatible with cryogenic environments [45]. Electronic tunability can be introduced to existing Si_3N_4 microresonator designs by the monolithic integration of an aluminium-nitride (AlN) piezoelectric actuator onto the Si_3N_4 microresonator [43,44,46], as illustrated in Fig. 1(b). The application of a voltage to the actuator induces a mechanical stress, which alters the refractive index of the waveguide through the stress-optical effect [47], so inducing a shift in the resonance frequency of the cavity. Such a design has already been successfully implemented in the classical regime through demonstrations of voltage-controlled soliton initiation and stabilization [43], unidirectional flow of light (isolators) [48], and frequency-agile narrow-linewidth lasers [38]. There have also been further experiments with this type of technology, such as the recently implemented high-speed programmable Mach-Zehnder meshes using AlN piezoelectric actuators coupled to Si_3N_4 waveguides [45]. However, up until this work, electronic tuning of photon frequencies generated by such microresonators has still not been investigated.

This paper reports on a piezoelectric-controlled frequency-tunable source of entangled photon pairs, based on Si_3N_4 microresonators. The results show these microresonators have the ability for fast electronic frequency tuning of entangled photon pairs, as well as high bandwidth locking to external lasers. This will be invaluable in the move towards interfacing with quantum memory platforms in the near future.

II. MATERIALS AND METHODS

Figure 1(a) shows a schematic of the tunable photon-pair source. The microresonators are based on Si_3N_4, shown as the black layer in Fig. 1(b), with a silica cladding (green), and are fabricated using the photonic Damascene process [51]. The cladding layer is made to be sufficiently thick to ensure that the optical field is negligible at the top of the cladding layer, so preserving the low optical propagation loss of the Si_3N_4 waveguide [51]. A layer of molybdenum (red) is deposited on the top silica cladding to act as the ground electrode, the AlN piezoelectric actuator (dark blue) is the main piezoelectric material (thickness 1 μm), with a final layer of molybdenum added to act as the top electrode. A detailed description of the chip design and fabrication process is given in Ref. [44]. The piezoelectric control is induced through the quasistatic stress-optic effect, causing strain in the amorphous Si_3N_4 waveguide and inducing changes in the refractive index of the Si_3N_4 [47]. This stress can be compressive or tensile, leading to either an increase or decrease in the local refractive index, and consequently an increase or decrease in the resonance frequency of the microresonator. Figure 1(c) shows a microscope image of the electrically wire bonded AlN actuator on top of the Si_3N_4 microresonator, with Fig. 1(d) showing a photograph of the optically and electrically packaged chip.

To demonstrate the frequency tuning capabilities of these devices, an initial characterization was implemented using the scheme illustrated in Fig. 2. A cw laser at 1555.7 nm passes through an electro-optic phase modulator (EOM) used to generate a Pound-Drever-Hall (PDH) error signal [52] for stabilization of the laser frequency to the microresonator. The light then passes through a polarization control stage to align the polarization with the quasitransverse electric (TE) mode of the microresonator, and filtering stages to ensure a clean pump spectrum reaches the chip. Following this, the 1% line from a 99:1 beam splitter goes to a photodiode which is used to monitor the input power. The remaining 99% is coupled directly into the bus waveguide on the chip through an ultrahigh numerical aperture (UHNA) fiber pigtailed to the chip. When the laser is brought on resonance, the laser couples evanescently into the microresonator via the bus waveguide, generating signal and idler photons through spontaneous four wave mixing (SFWM) at each mode supported by the cavity. This leads to the generation of a photon frequency comb with a frequency spacing ∼200 GHz, corresponding to the free spectral range (FSR) of the microresonator. The device itself is an overcoupled device with an average intrinsic linewidth ∼40 MHz and total linewidth ∼200 MHz. The chip temperature is stabilized at 297.32 K to within ±10 mK, using an active proportional-integral-derivative (PID) stabilization system, which feeds back to a peltier on which the chip is mounted. The photons couple out of the ring back to the bus waveguide and out of the chip, again through a UHNA fiber pigtailed to the chip. The 1% line of a second 99:1 beam splitter goes to a second photodiode for power monitoring. Five dense wavelength division multiplexers (DWDMs)—FSR = 200 GHz, channel 27—suppress the residual pump light, with the resulting signal and idler photons passing through a tunable narrow-band filter (bandwidth of 70 pm), being detected with in-house-developed superconducting nanowire single photon detectors (SNSPDs) [49,50]. By simultaneously changing the frequency of the tunable filter and each time acquiring photon counts, a spectrum of the photon frequency comb can be acquired.

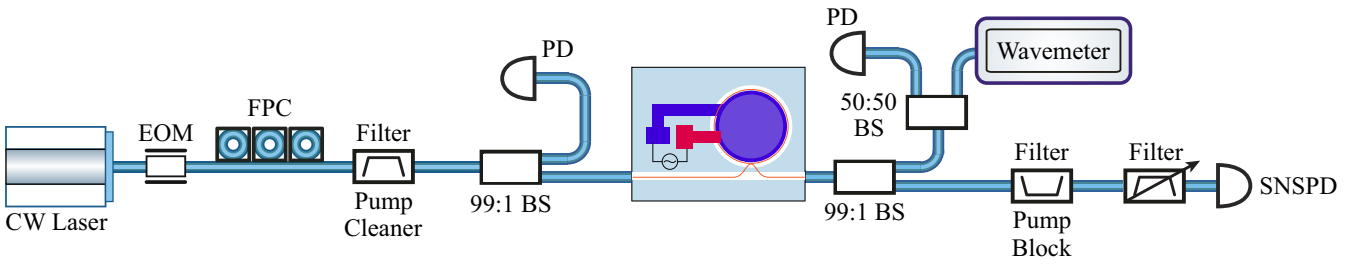

FIG. 2. Illustration of the basic experimental setup. The first filter before the microresonator is a dense wavelength division multiplexer (DWDM) centered at 1555.75 nm (channel 27, 200 GHz bandwidth) to provide a clean pump spectrum. The chip is mounted on a peltier which provides active temperature stabilization to within ±10 mK. Ultra-high numerical aperture (UHNA) fibers are pigtailed to the input and output of the bus waveguide on the chip. The pump block filter after the microresonator is comprised of a set of 5 DWDMs to suppress the residual pump, and the tunable filter has a bandwidth of 70 pm. Photons are detected using in-house developed SNSPDs [49,50]. Photodiodes provide both power monitoring and a locking signal for the frequency stabilization. EOM: electro-optic modulator, FPC: fiber polarization controller, BS: beam splitter, PD: photodiode, SNSPD: superconducting nanowire single photon detector.

A measurement of this frequency comb is shown in Fig. 3(a) (top). See Appendix A for further quantities characterizing the source.

III. RESULTS

By applying a voltage to the actuator, the frequencies of the modes supported by the microresonator (and hence the photon frequency comb) shift by a set amount. This shift was measured by scanning the tunable filter over a single-photon peak for different applied voltages. Figure 3(a) shows such single-photon peaks for two different applied voltages. It can be seen that the application of 30 V induces a shift of approximately 600 MHz. Figure 3(b) shows these frequency shifts as a function of the applied voltage, with an average linear tuning coefficient of 22.5 MHz V^{-1}. A single experiment cycle consisted of measuring the induced frequency shift for increasing voltages up to 30 V, followed immediately by measuring the shift for decreasing voltages back to 0 V. Small, linear drifts in the microresonator resonance frequency were observed due to changes in the ambient temperature over the long timescales of each experiment cycle. These were measured before and after each experiment cycle by sending part of the residual pump light after the microresonator to a wavemeter. The average of these drifts was consequently subtracted from the measurement cycle occurring in between. A slight hysteresis is observed, consistent with that seen in Ref. [43], which is most likely due to trapped charges [53].

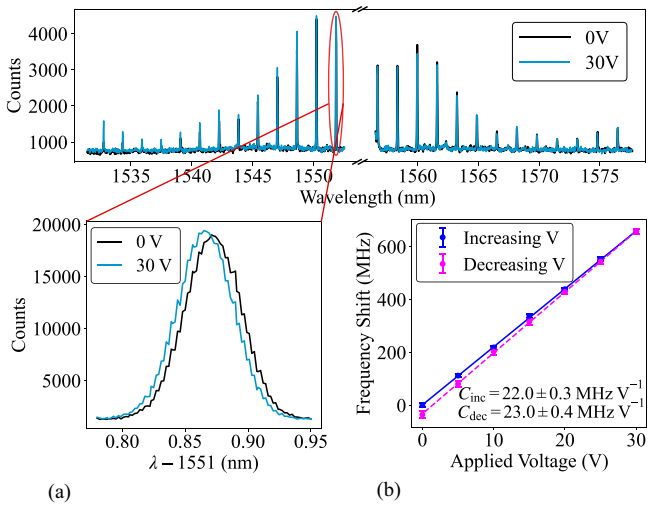

FIG. 3. Top: Correlated photon pairs generated by the Si_3N_4 microresonator for two different applied voltages, 0 V (black) and 30 V (light blue/light gray). The photon pairs form a frequency comb structure corresponding to the resonances of the cavity around the pump frequency. (a) Measurement of the wavelength λ of a single-photon peak (closest signal photon to the pump, red ellipse) for applied voltages of 0 V and 30 V. (b) Graph of the measured single-photon frequency shift as a function of applied voltage. A slight hysteresis is observed between the measured shift when increasing the voltage (blue/dark gray) and when decreasing the voltage (dashed pink/light gray). The extracted tuning coefficients from weighted fits are $C_{inc} = 22.0 \pm 0.3$ MHz V^{-1} for the increasing voltage, and $C_{dec} = 23.0 \pm 0.4$ MHz V^{-1} for the decreasing voltage. The shift was extracted through a Gaussian fit to the single-photon peak. Error bars are the standard error from the fit.

A. Bandwidth invariance

Quantities such as the photon bandwidth are dependent on the refractive index of the cavity material, with FWHM $\propto 1/n_g$, where FWHM is the full width at half maximum of the cavity resonance and n_g the group refractive index [54]. It is therefore natural to question whether there will be a significant change in the photon bandwidth with the applied voltage (as the voltage induces changes in the refractive index of the cavity). This is of particular importance when interfacing with rare-earth-ion quantum memories, where the photon bandwidths generated by the microresonator should match the absorption profile of the memory and remain constant irrespective of any applied voltage. If the photon bandwidths change such that they increase above that of the memory, then the memory would begin to act as a filter, with consequently fewer photons stored [55]. This would lead to a decrease in the so-called heralding efficiency, which is the efficiency with which the photon stored by the memory is "heralded" by detection of its partner photon [30]. To experimentally measure whether the photon bandwidths are voltage dependent, a 50:50

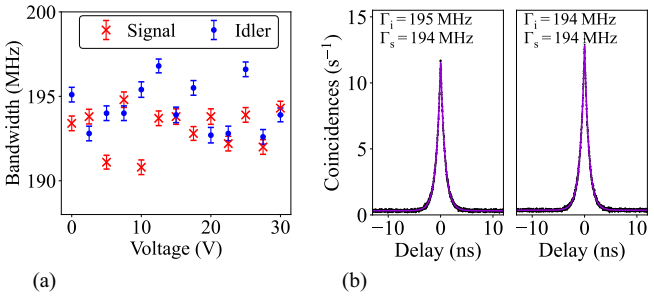

FIG. 4. (a) Bandwidth of the signal (red crosses) and idler (blue dots) photons as a function of applied voltage. The bandwidth is extracted directly from the linewidth of the signal-idler coincidence peak. Error bars are the standard error. (b) Signal-idler coincidence peaks for applied voltages of 0 V and 30 V. The linewidth of both the signal and idler photons $\Gamma_{s,i}$ are ∼194 MHz for both voltages.

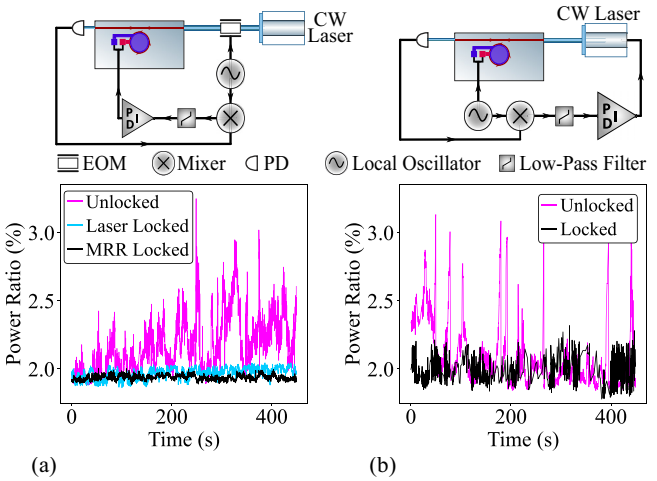

FIG. 5. Comparison of transmitted power ratio for unlocked and locked circuits. Above each graph, an illustration of the relevant locking circuit is shown. (a) For modulation of the EOM, a comparison of the unlocked (magenta, uppermost trace) and locked (black) cases is shown when the locking signal is fed back to the chip, as shown in the illustration. The power ratio when the locking signal is fed back to the laser (blue/light gray) is also shown for comparison. (b) For microresonator modulation, a comparison of the unlocked (magenta/gray) and locked (black) cases is shown, with the locking signal subsequently fed back to the laser.

beam splitter was included after the pump suppression filter in the setup shown in Fig. 2, with each arm passing through a tunable filter set to either the signal or idler wavelength. Each arm then goes to its own SNSPD, with the coincidences between detections subsequently recorded. Examples of the signal-idler coincidences recorded from this setup are shown in Fig. 4(b) for two different voltages applied to the AlN layer. The photon bandwidth can then be directly extracted as the linewidth of the signal-idler coincidence peak. The coincidence peak is fitted using a convolution of a double-exponential decay convolved with a Gaussian [28]. This takes into account the temporal shape of each photon (defined by the cavity), along with the temporal jitter introduced from the SNSPDs, which is a Gaussian distribution [49]. Note that the detector jitter is much smaller than the bandwidth of the photons.

The measured bandwidth of the signal and idler photons as a function of the applied voltage is shown in Fig. 4(a). It can be seen from the figure that there appears to be no measurable correlation between the bandwidth of the photons and the voltage applied to the microresonator. To confirm that the scatter seen in the figure is also not significant, the overlap between two wave packets which are assumed to differ in bandwidth by the maximum scatter of 10 MHz seen in Fig. 4(a) can be calculated, and is found to be ∼99.9% [56,57]. From this, it can be concluded that there should be no effect on the heralding efficiency from application of voltages to the resonator.

B. Frequency stabilization of the microresonator

When interfacing these microresonator photon sources with quantum memories and moving towards a future quantum repeater-like implementation, the photon frequency must be resonant with the quantum memory at all times. As such, a frequency-locking scheme will be needed to lock the resonance of the microresonator to the frequency of the quantum memory. There have been previous demonstrations of frequency-locking microresonators by feeding back a locking signal to the temperature of the microresonators, however the achievable locking bandwidth in such schemes is very small, previously reported to be only in the tens of Hertz regime [58–61] (although the actuation bandwidth is much higher [41,42]). Focus has therefore moved away from such thermal locking schemes, with recent developments including piezoelectric frequency-locking schemes integrated on-chip [62]. However, the use of such devices as photon-pair sources has not yet been demonstrated.

With the AlN integrated microresonator devices, it is possible to lock the cavity resonance to the pump laser using the PDH technique [52] and feeding back the signal to the AlN layer [43]. A schematic of this scheme is shown in Fig. 5(a). An error signal was generated by sending a local oscillator modulation signal to an external EOM and monitoring the residual pump light transmitted by the microresonator when on resonance with the laser, using a photodiode. The resultant optical modulation will either be in phase or out of phase with the applied local oscillator modulation, depending on whether the laser frequency is positively or negatively detuned from the resonance frequency. By mixing the resulting optical modulation signal with the applied local oscillator, and passing the signal through a low-pass filter in order to suppress higher-order frequency components, an asymmetric error signal is obtained, which can be passed to a PID servo loop. The resultant voltage from the PID servo loop was subsequently applied to the AlN layer on top of the microresonator cavity, so adjusting the frequency of the cavity such that it remained resonant with the pump laser. This scheme mimics that which will be needed to keep the microresonator resonant with a quantum memory in the future.

Figure 5(a) shows the results from this locking scheme. The plot shows the power ratio, which is the ratio of the transmitted pump power after the microresonator to the input power of the microresonator. The power ratio provides an

indication of the stability of the laser with respect to the microresonator resonance as, at the point of resonance, it will be at a minimum. Deviations away from this point cause the power ratio to increase. Shown in magenta (uppermost trace) is the power ratio for the unlocked resonance, where large fluctuations can be seen as the laser drifts in and out of resonance with the microresonator. The locked case is shown in black, where the power ratio is extremely stable in comparison. For further comparison, the locked case when the locking signal is instead fed back to the laser (rather than the AlN layer) is shown in blue (light gray). The implementation of this system allowed the chip to remain on resonance with the laser for in excess of 16 h. The system eventually fell out of lock when the locking circuit reached its maximum value of 30 V (that is, to keep the chip on resonance with the laser, the circuit would have had to provide more than 30 V). Even though AlN itself can sustain in excess of ±100 V [43], in this case the maximum was restricted to 30 V in order to avoid damage to the wirebonds attached to the chip. This experiment demonstrates that we have a source of photon pairs which can be frequency stabilized to an external reference laser, compatible with the requirements for some quantum memory schemes [8].

C. Microresonator-modulated locking

The technique of modulating an external EOM to implement a PDH lock has been widely implemented for many decades, however there also exist extensions to the original proposal where the modulation signal is applied to different (potentially integrated) components. For example, Padmaraju *et al.* [58,59] have previously implemented a scheme whereby the modulation signal is applied to the microresonator itself via a resistive heater. There are limitations to the locking bandwidth of this implementation, however, primarily due to the slow thermal response of the chip [58,59]. With the microresonators presented here, a modulation signal can instead be applied to the piezoelectric layer, as demonstrated in similar scenarios in Refs. [43,62]. This leads to a modulation of the optical signal and the derivation of a PDH error signal which can be used to lock the pump laser to the microresonator, as shown in the schematic in Fig. 5(b). The plot in Fig. 5(b) shows power ratio measurements for the unlocked case where the microresonator was modulated at 40 MHz, and for the locked case, again with the microresonator modulated at 40 MHz. Although noisier than when modulating the external EOM, it can clearly be seen that the laser is kept on resonance with the chip throughout the measurement, in contrast to the unlocked case where it drifts in and out. The increased noise is likely due to the suboptimal locking regime which had to be used to implement this scheme—see Appendix B for further information. This demonstration of microresonator-modulated fast-frequency locking shows the potential use of this technology in the future for removing the need for often-expensive EOMs, which are also not necessarily available at all required wavelengths.

D. Locking bandwidth

Finally, to measure the response of the microresonator-locking system [schematic in Fig. 5(a)] to noise, an external noise process was introduced to the system by applying a linear frequency sweep to the laser current, with part of the output from the microresonator monitored by a photodiode. Figure 6(a) shows the measured spectral power from the fast Fourier transform (FFT) of the photodiode signal for the unlocked (black) and locked (blue/light gray) systems with a noise sweep from 1 Hz to 1 kHz (a Gaussian filter was applied to the data to better resolve the characteristics). Overall, the intensity noise is suppressed by a factor of ∼8 dB in this region. However, there are also several noise spikes which are suppressed by a factor well in excess of this. By driving the system with increasingly higher noise frequencies, this allowed an estimation of the bandwidth of the entire locking circuit (an amalgamation of the response of the microresonator AlN layer and the electronic circuitry) to be made. By looking for the point at which the unlocked and locked spectral powers overlap, the noise bandwidth that the entire circuit can suppress can be estimated. Figure 6(b) shows three graphs around this point of interest: The upper plot shows the noise regime from 99.5 kHz to 100.5 kHz, where the locked circuit still gives slight suppression of the noise compared to the unlocked circuit. The middle plot shows the regime from 103.5 kHz to 105.5 kHz, where the two circuits are the same. The bottom plot shows the regime from 107 kHz to 108 kHz, where the locked case actually has a higher noise level than the unlocked case. From this, the locking bandwidth can be estimated to be on the order of 100 kHz. This is a vast improvement on those schemes which use the thermal response of the chip for stabilization, with previous reports only reaching bandwidths on the order of tens of Hertz [58–60].

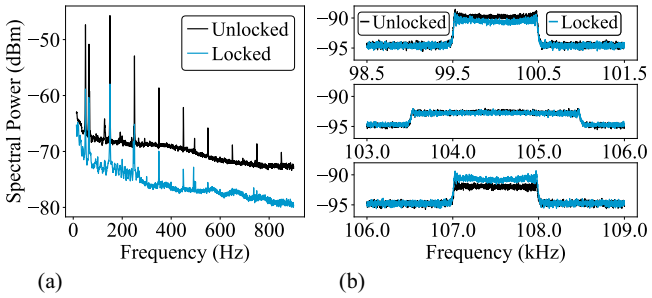

FIG. 6. Measured spectral power after the microresonator for both unlocked (black) and locked (blue/light gray) circuits. (a) Measured spectral power for low frequencies. (b) Determination of locking bandwidth using the measured spectral power for several higher frequencies. Shown is the point below crossing (top), at the point of crossing (middle), and above crossing (bottom). See text for further details. A Gaussian filter was applied to the data to better resolve the characteristics.

IV. CONCLUSION

This work has demonstrated the suitability of these Si_3N_4-based microresonators, with monolithically integrated piezoelectric actuators, as frequency-tunable photon-pair sources. It has shown that they continue to produce narrow-linewidth photon pairs comparable to previous state-of-the-art sources which lack such piezoelectric-controlled frequency tunability. They provide reliable, voltage-controlled frequency tuning

of the generated photon pairs, as well as allowing for PDH locking with bandwidths far in excess of those achievable using temperature locking. These abilities add to the existing "photonic toolbox" available when using such integrated microresonators as photon-pair sources, and will have direct application when interfacing with quantum memories based on trapped-ion or rare-earth-ion schemes in the near future. In particular, the bandwidths currently achievable with these devices are comparable to some quantum memories, such as those based on rare-earth-ion schemes [8]. In addition, due to the wide transparency window of Si_3N_4 [37], a large number of atomic transitions have the potential to be accessed. Successful visible-telecom photon generation using Si_3N_4 microresonators has already been demonstrated [63] and so, with further engineering, the tunable devices presented here are expected to be able to generate photon pairs bridging the visible-telecom wavelength regime. In combination with the fast-frequency actuation presented in this work, such developments will allow interfacing of these devices with rare-earth-ion quantum memories, paving the way for implementation of repeater-like links for quantum networks.

ACKNOWLEDGMENTS

The authors would like to thank L. Stasi and G. V. Resta for development, maintenance, and technical support of the SNSPDs and cryostats, and C. Barreiro for electronic support. The authors would also like to thank A. Toros, V. Shadymov, and A. Voloshin for assistance in wirebonding. T.B. would like to thank J. A. Harrington for useful discussions. The chip samples were fabricated in the EPFL Center of MicroNanoTechnology (CMi), and in the Birck Nanotechnology Center at Purdue University. AlN deposition was performed at OEM Group Inc. This work was supported by Swiss National Science Foundation (SNSF) Grants No. 200020_182664 and No. 192293, the NCCR QSIT, and Contract No. W911NF2120248 (NINJA) from the Defense Advanced Research Projects Agency (DARPA), Microsystems Technology Office (MTO). A.S. acknowledges support from the European Space Technology Center with ESA Contract No. 4000135357/21/NL/GLC/my.

APPENDIX A: CHARACTERISTICS OF THE MICRORESONATOR PHOTON-PAIR SOURCE

This section presents characteristics of the voltage-controlled, frequency-tunable microresonator photon-pair source.

The Si_3N_4 microresonator has waveguides of 2.2 μm width and 900 nm height, with an AlN layer of thickness 1 μm. It is an overcoupled device, with $\kappa_{ex} \approx 3 \times \kappa_0$, where κ_{ex} is the external coupling rate from the bus waveguide to the cavity, and κ_0 corresponds to the intrinsic linewidth of the cavity. This leads to an improved extraction efficiency, with the device having an average intrinsic linewidth ~40 MHz and total linewidth ~200 MHz.

Figures 7(a) and 7(b) show a photograph of the electrical and optical packaging of the chip. The UHNA fibers are pigtailed to the chip using epoxy. The electrical wirebonds are made from 17-μm-diameter aluminium. Figures 7(c) and 7(d) show the optomechanical frequency response $S_{21}(\omega)$ of

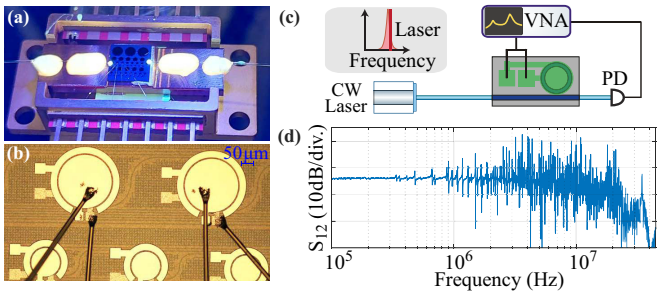

FIG. 7. (a) Photograph of the electrically and optically packaged chip. The fibers are pigtailed to the chip using epoxy. (b) Microscope image of the electrically wire-bonded AlN actuator on top of the Si_3N_4 microresonator. (c) and (d) Optomechanical frequency response $S_{21}(\omega)$ of the microresonator when modulated at frequency ω. (c) Experimental scheme used to measure the optomechanical frequency response. (d) Experimental results from a microresonator similar to the device used throughout this work, except without optical packaging. VNA: vector network analyzer, PD: photodiode.

a similar device when a modulation at frequency ω is applied to the AlN layer of the microresonator (i.e., a measure of the electrical to optical transduction). The experimental setup of the actuation response measurement is shown in Fig. 7(c). An actuation voltage at frequency ω is generated from a vector network analyzer (VNA) and applied to the piezoactuator on the chip. The pump laser frequency is tuned to the slope of the Si_3N_4 microresonator resonance, with a photodiode detecting the optical signal containing the modulation. Figure 7(d) shows the measured optomechanical $S_{21}(\omega)$ response of a tunable microresonator device similar to that used throughout this work, except without optical packaging. The actuation applied to the AlN piezoelectric layer excites many mechanical bulk or contour modes of the photonic chip, leading to a nonflat actuation response. It can be seen that the response

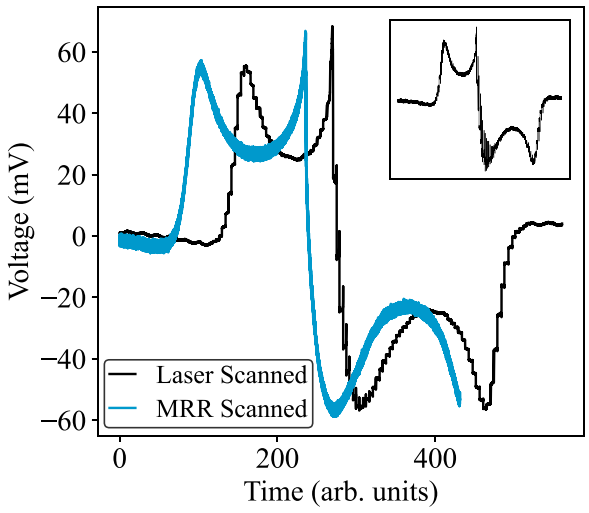

FIG. 8. Oscilloscope trace of the error signals generated when a local oscillator is applied to an external EOM. In black (rightmost trace), the laser piezo was scanned over the microresonator point of resonance. In blue (gray, leftmost trace), the microresonator point of resonance was scanned over the laser frequency. Inset: Unsmoothed data. Data was smoothed by a polynomial of order seven in order to remove noise present from the laser's piezo.

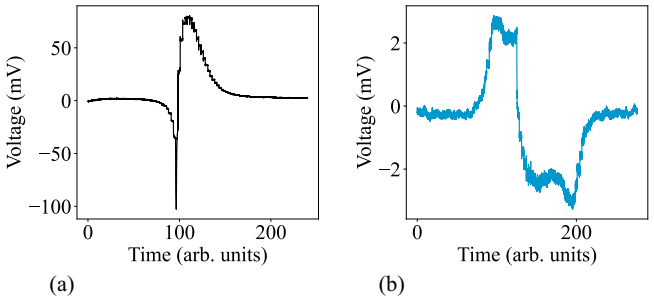

FIG. 9. Oscilloscope traces of error signals generated when applying a modulation signal to the microresonator itself, and scanning the laser piezo over the point of resonance. (a) Error signal when the microresonator is modulated by a signal of 40 MHz. (b) Error signal when the microresonator is modulated by a signal of 411 MHz. Note the difference in voltage scale between this plot and (b). Data was smoothed by a polynomial of order seven in order to remove noise present from the laser's piezo.

is flat up to 340 kHz, where the first mechanical resonance is visible. Note that these mechanical modes can be suppressed via techniques such as mode cancellation, apodization, or by using an acoustic absorber such as carbon tape or a glass submount [64].

The bandwidth of the photon pairs (shown in Fig. 4 of the main text) gives an indication of the Q-factor of the microresonator. For the microresonator used in this work, the Q-factor was calculated to be $\sim 1 \times 10^6$ (equivalent to an average photon bandwidth of 194 MHz), comparable to many state-of-the art Si_3N_4 photon-pair sources [65].

The intracavity pair generation rate (PGR), defined as

$$\mathrm{PGR} = \frac{S_\mathrm{i} S_\mathrm{s}}{R_\mathrm{cc}}, \tag{A1}$$

with $S_{\mathrm{i(s)}}$ the single-photon count rates for the idler(signal) photons and R_cc the coincidence rate, was found to be on the order of $\mathrm{PGR} = 32 \times 10^3\,\mathrm{s}^{-1}\,\mathrm{mW}^{-2}$. This is comparable to many other microresonator photon pair sources which lack the voltage-controllable frequency tunability of these devices, such as those in Refs. [28,66]. For the results shown in Fig. 4(a) of the main text, with an average measured bandwidth of 194 MHz, this results in a probability of pair generation per coherence time of $p = 0.01$.

The heralding efficiency, defined by

$$\eta_{\mathrm{h,i(s)}} = \frac{R_\mathrm{cc}}{S_{\mathrm{s(i)}}\eta_\mathrm{d}}, \tag{A2}$$

is found to be, on average, $\eta_\mathrm{h} = 1.6\%$ for both signal and idler, using a detector efficiency of $\eta_\mathrm{d} = 0.84$ for both detectors. As the aim of this work is to demonstrate the frequency-tuning capabilities of the photon-pair source, and not to optimize photon-pair production, a large number of DWDMs were used, as well as relatively high-loss tunable filters. Therefore, a more useful measure is the coupling efficiency from the chip into the UHNA fiber. The coupling efficiency is given by

$$\eta_{\mathrm{coup,i(s)}} = \frac{R_\mathrm{cc}}{S_{\mathrm{s(i)}}\eta_\mathrm{d} t_{\mathrm{i(s)}}}, \tag{A3}$$

where $t_{\mathrm{s(i)}}$ is the overall transmission from the output of the UHNA fiber pigtailed to the chip to the detector for the signal(idler) path. The average coupling efficiency was found to be $\eta_\mathrm{coup} = 14.7\%$ for both signal and idler.

Improvements to the heralding efficiency could be straightforwardly implemented by replacing the tunable filters with fixed-frequency DWDMs at channels corresponding to appropriate signal(idler) generation wavelengths. However, these were not used here in order to allow for scanning over the photon frequencies to measure the relevant shifts induced by voltages applied to the microresonator.

APPENDIX B: CHARACTERISTICS OF THE LOCKING SCHEMES

Figure 8 shows the error signals generated when a modulation frequency of 846.6 MHZ is applied to an external EOM. Shown in black (rightmost trace) is the signal extracted when a laser piezo is scanned over the microresonator point of resonance. As the laser piezo introduced noise spikes to the error signal (inset), the data was smoothed using a seventh-order polynomial to better see the signal characteristics. In blue (gray, leftmost trace) is shown the error signal extracted when instead the microresonator is scanned, through application of a voltage to the AlN layer, over the laser frequency. The overall characteristics of the two error signals can be seen to be identical.

Figures 9(a) and 9(b) show the error signals extracted by applying a modulation signal to the microresonator itself at two different frequencies, while simultaneously scanning the laser frequency over the point of resonance. In the ideal locking regime, the microresonator would be modulated at a frequency much larger than the resonance frequency (e.g., at a frequency similar to the 846.6 MHz applied to the external EOM). However, it can be seen from Fig. 9(b) that at higher modulation frequencies, the amplitude of the error signal is significantly reduced compared to lower frequencies. As such, a lower modulation frequency had to be used for locking of the laser to the microresonator for the microresonator-modulated case than with the EOM. It is likely that this suboptimal locking regime contributes to the increased fluctuations present in the locked power ratio shown in Fig. 5(b) of the main text. If a high-frequency modulation was chosen to coincide with a high-overtone bulk acoustic resonator (HBAR) mode of the chip, it is likely that the amplitude of the error signal would be greatly enhanced, as shown previously in Ref. [43].

[1] N. Gisin and R. Thew, Quantum communication, Nat. Photonics **1**, 165 (2007).

[2] M. Krenn, M. Malik, T. Scheidl, R. Ursin, and A. Zeilinger, Quantum communication with photons, in *Optics in Our Time*, edited by M. Al-Amri, M. El-Gomati, and M. Zubairy (Springer International Publishing, Cham, 2016) pp. 455–482.

[3] N. Sangouard, C. Simon, H. de Riedmatten, and N. Gisin, Quantum repeaters based on atomic ensembles and linear optics, Rev. Mod. Phys. **83**, 33 (2011).

[4] S. Wehner, D. Elkouss, and R. Hanson, Quantum internet: A vision for the road ahead, Science **362**, eaam9288 (2018).

[5] S. Slussarenko and G. J. Pryde, Photonic quantum information processing: A concise review, Appl. Phys. Rev. **6**, 041303 (2019).

[6] H.-S. Zhong, H. Wang, Y.-H. Deng, M.-C. Chen, L.-C. Peng, Y.-H. Luo, J. Qin, D. Wu, X. Ding, Y. Hu *et al.*, Quantum computational advantage using photons, Science **370**, 1460 (2020).

[7] C. Simon, M. Afzelius, J. Appel, A. Boyer de la Giroday, S. J. Dewhurst, N. Gisin, C. Y. Hu, F. Jelezko, S. Kröll, J. H. Muller *et al.*, Quantum memories: A review based on the European integrated project "Qubit Applications (QAP)," Eur. Phys. J. D **58**, 1 (2010).

[8] M. Businger, A. Tiranov, K. T. Kaczmarek, S. Welinski, Z. Zhang, A. Ferrier, P. Goldner, and M. Afzelius, Optical Spin-Wave Storage in a Solid-State Hybridized Electron-Nuclear Spin Ensemble, Phys. Rev. Lett. **124**, 053606 (2020).

[9] M. F. Askarani, A. Das, J. H. Davidson, G. C. Amaral, N. Sinclair, J. A. Slater, S. Marzban, C. W. Thiel, R. L. Cone, D. Oblak, and W. Tittel, Long-Lived Solid-State Optical Memory for High-Rate Quantum Repeaters, Phys. Rev. Lett. **127**, 220502 (2021).

[10] C. D. Bruzewicz, J. Chiaverini, R. McConnell, and J. M. Saged, Trapped-ion quantum computing: Progress and challenges, Appl. Phys. Rev. **6**, 021314 (2019).

[11] T. Brydges, A. Elben, P. Jurcevic, B. Vermersch, C. Maier, B. P. Lanyon, P. Zoller, R. Blatt, and C. Roos, Probing Rényi entanglement entropy via randomized measurements, Science **364**, 260 (2019).

[12] V. Krutyanskiy, M. Galli, V. Krcmarsky, S. Baier, D. A. Fioretto, Y. Pu, A. Mazloom, P. Sekatski, M. Canteri, M. Teller, J. Schupp, J. Bate, M. Meraner, N. Sangouard, B. P. Lanyon, and T. E. Northup, Entanglement of Trapped-Ion Qubits Separated by 230 Meters, Phys. Rev. Lett. **130**, 050803 (2023).

[13] H. Bernien, B. Hensen, W. Pfaff, G. Koolstra, M. S. Blok, L. Robledo, T. H. Taminiau, M. Markham, D. J. Twitchen, L. Childress, and R. Hanson, Heralded entanglement between solid-state qubits separated by three metres, Nature (London) **497**, 86 (2013).

[14] M. Pompili, S. L. N. Hermans, S. Baier, H. K. C. Beukers, P. C. Humphreys, R. N. Schouten, R. F. L. Vermeulen, M. J. Tiggelman, L. dos Santos Martins, B. Dirkse, S. Wehner, and R. Hanson, Realization of a multinode quantum network of remote solid-state qubits, Science **372**, 259 (2021).

[15] G. Moody, V. J. Sorger, D. J. Blumenthal, P. W. Juodawlkis, W. Loh, C. Sorace-Agaskar, A. E. Jones, K. C. Balram, J. C. F. Matthews, A. Laing *et al.*, 2022 Roadmap on integrated quantum photonics, J. Phys. Photonics **4**, 012501 (2022).

[16] P. Marin-Palomo, J. N. Kemal, M. Karpov, A. Kordts, J. Pfeifle, M. H. P. Pfeiffer, P. Trocha, S. Wolf, V. Brasch, M. H. Anderson, R. Rosenberger, K. Vijayan, W. Freude, T. J. Kippenberg, and C. Koos, Microresonator-based solitons for massively parallel coherent optical communications, Nature (London) **546**, 274 (2017).

[17] A. Singh, Q. Li, S. Liu, Y. Yu, X. Lu, C. Schneider, S. Höfling, J. Lawall, V. Verma, R. Mirin, S. W. Nam, J. Liu, and K. Srinivasan, Quantum frequency conversion of a quantum dot single-photon source on a nanophotonic chip, Optica **6**, 563 (2019).

[18] T. J. Kippenberg, A. L. Gaeta, M. Lipson, and M. L. Gorodetsky, Dissipative Kerr solitons in optical microresonators, Science **361**, eaan8083 (2018).

[19] E. Engin, D. Bonneau, C. M. Natarajan, A. S. Clark, M. G. Tanner, R. H. Hadfield, S. N. Dorenbos, V. Zwiller, K. Ohira, N. Suzuki, H. Yoshida, N. Iizuka, M. Ezaki, J. L. O'Brien, and M. G. Thompson, Photon pair generation in a silicon micro-ring resonator with reverse bias enhancement, Opt. Express **21**, 27826 (2013).

[20] J. Silverstone, R. Santagati, D. Bonneau, M. Strain, M. Sorel, J. O'Brien, and M. Thompson, Qubit entanglement between ring-resonator photon-pair sources on a silicon chip, Nat. Commun. **6**, 7948 (2015).

[21] C. Reimer, M. Kues, P. Roztocki, B. Wetzel, F. Grazioso, B. E. Little, S. T. Chu, T. Johnston, Y. Bromberg, L. Caspani, D. J. Moss, and R. Morandotti, Generation of multiphoton entangled quantum states by means of integrated frequency combs, Science **351**, 1176 (2016).

[22] X. Guo, C.-L. Zou, C. Schuck, H. Jung, R. Cheng, and H. X. Tang, Parametric down-conversion photon-pair source on a nanophotonic chip, Light Sci. Appl. **6**, e16249 (2017).

[23] I. I. Faruque, G. F. Sinclair, D. Bonneau, J. G. Rarity, and M. G. Thompson, On-chip quantum interference with heralded photons from two independent micro-ring resonator sources in silicon photonics, Opt. Express **26**, 20379 (2018).

[24] F. Samara, A. Martin, C. Autebert, M. Karpov, T. J. Kippenberg, H. Zbinden, and R. Thew, High-rate photon pairs and sequential time-bin entanglement with Si_3N_4 microring resonators, Opt. Express **27**, 19309 (2019).

[25] Z. Ma, J.-Y. Chen, Z. Li, C. Tang, Y. M. Sua, H. Fan, and Y.-P. Huang, Ultrabright Quantum Photon Sources on Chip, Phys. Rev. Lett. **125**, 263602 (2020).

[26] D. Oser, S. Tanzilli, F. Mazeas, C. Alonso-Ramos, X. L. Roux, G. Sauder, X. Hua, O. Alibart, L. Vivien, E. Cassan, and L. Labonté, High-quality photonic entanglement out of a stand-alone silicon chip, Npj Quantum Inf. **6**, 31 (2020).

[27] F. Samara, N. Maring, A. Martin, A. S. Raja, T. J. Kippenberg, H. Zbinden, and R. Thew, Entanglement swapping between independent and asynchronous integrated photon-pair sources, Quantum Sci. Technol. **6**, 045024 (2021).

[28] F. Samara, Integrated Si_3N_4 Microring Resonator: A Photon-Pair Source for Quantum Communication, Ph.D. thesis, University of Geneva, 2021.

[29] T. J. Steiner, J. E. Castro, L. Chang, Q. Dang, W. Xie, J. Norman, J. E. Bowers, and G. Moody, Ultrabright entangled-photon-pair generation from an AlGaAs-on-insulator microring resonator, PRX Quantum **2**, 010337 (2021).

[30] D. Lago-Rivera, S. Grandi, J. V. Rakonjac, A. Seri, and H. de Riedmatten, Telecom-heralded entanglement between multimode solid-state quantum memories, Nature (London) **594**, 37 (2021).

[31] X.-L. Wang, L.-K. Chen, W. Li, H.-L. Huang, C. Liu, C. Chen, Y.-H. Luo, Z.-E. Su, D. Wu, Z.-D. Li, H. Lu, Y. Hu, X. Jiang, C.-Z. Peng, L. Li, N.-L. Liu, Y.-A. Chen, C.-Y. Lu, and J.-W. Pan, Experimental Ten-Photon Entanglement, Phys. Rev. Lett. **117**, 210502 (2016).

[32] L.-K. Chen, Z.-D. Li, X.-C. Yao, M. Huang, W. Li, H. Lu, X. Yuan, Y.-B. Zhang, X. Jiang, C.-Z. Peng, L. Li, N.-L. Liu, X. Ma, C.-Y. Lu, Y.-A. Chen, and J.-W. Pan, Observation of

ten-photon entanglement using thin BiB_3O_6 crystals, Optica **4**, 77 (2017).

[33] E. Meyer-Scott, N. Montaut, J. Tiedau, L. Sansoni, H. Herrmann, T. J. Bartley, and C. Silberhorn, Limits on the heralding efficiencies and spectral purities of spectrally filtered single photons from photon-pair sources, Phys. Rev. A **95**, 061803(R) (2017).

[34] D. J. Blumenthal, R. Heideman, D. Geuzebroek, A. Leinse, and C. Roeloffzen, Silicon Nitride in Silicon Photonics, *Proceedings of the IEEE* (IEEE, New York, 2018) Vol. 106, pp. 2209–2231.

[35] J. Liu, G. Huang, R. N. Wang, J. He, A. S. Raja, T. Liu, N. J. Engelsen, and T. J. Kippenberg, High-yield, wafer-scale fabrication of ultralow-loss, dispersion-engineered silicon nitride photonic circuits, Nat. Commun. **12**, 2236 (2021).

[36] A. Rahim, E. Ryckeboer, A. Z. Subramanian, S. Clemmen, B. Kuyken, A. Dhakal, A. Raza, A. Hermans, M. Muneeb, S. Dhoore, Y. Li, U. Dave, P. Bienstman, N. L. Thomas, G. Roelkens, D. V. Thourhout, P. Helin, S. Severi, X. Rottenberg, and R. Baets, Expanding the silicon photonics portfolio with silicon nitride photonic integrated circuits, J. Lightwave Technol. **35**, 639 (2017).

[37] P. Muñoz, G. Micó, L. A. Bru, D. Pastor, D. Pérez, J. D. Doménech, J. Fernández, R. Baños, B. Gargallo, R. Alemany, A. M. Sánchez, J. M. Cirera, R. Mas, and C. Domínguez, Silicon nitride photonic integration platforms for visible, near-infrared and mid-infrared applications, Sensors **17**, 2088 (2017).

[38] G. Lihachev, J. Riemensberger, W. Weng, J. Liu, H. Tian, A. Siddharth, V. Snigirev, V. Shadymov, A. Voloshin, R. N. Wang *et al.*, Low-noise frequency-agile photonic integrated lasers for coherent ranging, Nat. Commun. **13**, 3522 (2022).

[39] Y. Liu, Z. Qiu, X. Ji, A. Lukashchuk, J. He, J. Riemensberger, M. Hafermann, R. N. Wang, J. Liu, C. Ronning, and T. J. Kippenberg, A photonic integrated circuit-based erbium-doped amplifier, Science **376**, 1309 (2022).

[40] R. R. Kumar, X. Wu, Y. Zhang, and H. K. Tsang, Integrated photon-pair generation and 112 dB pump rejection filters for silicon quantum photonics, *CLEO: Science and Innovations* (Optica Publishing Group, Washington, DC, 2020) pp. SM3O–2.

[41] X. Xue, Y. Xuan, C. Wang, P.-H. Wang, Y. Liu, B. Niu, D. E. Leaird, M. Qi, and A. M. Weiner, Thermal tuning of Kerr frequency combs in silicon nitride microring resonators, Opt. Express **24**, 687 (2016).

[42] C. Joshi, J. K. Jang, K. Luke, X. Ji, S. A. Miller, A. Klenner, Y. Okawachi, M. Lipson, and A. L. Gaeta, Thermally controlled comb generation and soliton modelocking in microresonators, Opt. Lett. **41**, 2565 (2016).

[43] J. Liu, H. Tian, E. Lucas, A. S. Raja, G. Lihachev, R. N. Wang, J. He, T. Liu, M. H. Anderson, W. Weng, S. A. Bhave, and T. J. Kippenberg, Monolithic piezoelectric control of soliton microcombs, Nature (London) **583**, 385 (2020).

[44] H. Tian, J. Liu, B. Dong, J. C. Skehan, M. Zervas, T. J. Kippenberg, and S. A. Bhave, Hybrid integrated photonics using bulk acoustic resonators, Nat. Commun. **11**, 3073 (2020).

[45] M. Dong, G. Clark, A. J. Leenheer, M. Zimmermann, D. Dominguez, A. J. Menssen, D. Heim, G. Gilbert, D. Englund, and M. Eichenfield, High-speed programmable photonic circuits in a cryogenically compatible, visible-near-infrared 200 mm CMOS architecture, Nat. Photon. **16**, 59 (2022).

[46] W. Jin, R. G. Polcawich, P. A. Morton, and J. E. Bowers, Piezoelectrically tuned silicon nitride ring resonator, Opt. Express **26**, 3174 (2018).

[47] P. J. M. van der Slot, M. A. G. Porcel, and K.-J. Boller, Surface acoustic waves for acousto-optic modulation in buried silicon nitride waveguides, Opt. Express **27**, 1433 (2019).

[48] H. Tian, J. Liu, A. Siddharth, R. N. Wang, T. Blésin, J. He, T. J. Kippenberg, and S. A. Bhave, Magnetic-free silicon nitride integrated optical isolator, Nat. Photonics **15**, 828 (2021).

[49] M. Caloz, M. Perrenoud, C. Autebert, B. Korzh, M. Weiss, C. Schönenberger, R. J. Warburton, H. Zbinden, and F. Bussières, High-detection efficiency and low-timing jitter with amorphous superconducting nanowire single-photon detectors, Appl. Phys. Rev. **112**, 061103 (2018).

[50] C. Autebert, G. Gras, E. Amri, M. Perrenoud, M. Caloz, H. Zbinden, and F. Bussières, Direct measurement of the recovery time of superconducting nanowire single-photon detectors, J. Appl. Phys. **128**, 074504 (2020).

[51] M. H. P. Pfeiffer, A. Kordts, V. Brasch, M. Zervas, M. Geiselmann, J. D. Jost, and T. J. Kippenberg, Photonic Damascene process for integrated high-Q microresonator based nonlinear photonics, Optica **3**, 20 (2016).

[52] R. W. P. Drever, J. L. Hall, F. V. Kowalski, J. Hough, G. M. Ford, A. J. Munley, and H. Ward, Laser phase and frequency stabilization using an optical resonator, Appl. Phys. B **31**, 97 (1983).

[53] C. Aardahl, J. Rogers, H. Yun, Y. Ono, D. Tweet, and S.-T. Hsu, Electrical properties of AlN thin films deposited at low temperature on Si(100), Thin Solid Films **346**, 174 (1999).

[54] W. Bogaerts, P. D. Heyn, T. V. Vaerenbergh, K. DeVos, S. K. Selvaraja, T. Claes, P. Dumon, P. Bienstman, D. V. Thourhout, and R. Baets, Silicon microring resonators, Laser Photonics Rev. **6**, 47 (2012).

[55] C. Clausen, F. Bussières, A. Tiranov, H. Herrmann, C. Silberhorn, W. Sohler, M. Afzelius, and N. Gisin, A source of polarization-entangled photon pairs interfacing quantum memories with telecom photons, New J. Phys. **16**, 093058 (2014).

[56] C. Santori, D. Fattal, J. Vučković, G. S. Solomon, and Y. Yamamoto, Indistinguishable photons from a single-photon device, Nature (London) **419**, 594 (2002).

[57] L. Yu, C. M. Natarajan, T. Horikiri, C. Langrock, J. S. Pelc, M. G. Tanner, E. Abe, S. Maier, C. Schneider, S. Höfling, M. Kamp, R. H. Hadfield, M. M. Fejer, and Y. Yamamoto, Two-photon interference at telecom wavelengths for time-bin-encoded single photons from quantum-dot spin qubits, Nat. Commun. **6**, 8955 (2015).

[58] K. Padmaraju, D. F. Logan, T. Shiraishi, J. J. Ackert, A. P. Knights, and K. Bergman, Wavelength locking and thermally stabilizing microring resonators using dithering signals, J. Light. Technol. **32**, 505 (2014).

[59] X. Zhu, K. Padmaraju, L.-W. Luo, M. Glick, R. Dutt, M. Lipson, and K. Bergman, Fast wavelength locking of a microring resonator, *2014 Optical Interconnects Conference* (IEEE, New York, 2014) pp. 11–12.

[60] R. Zektzer, L. Stern, N. Mazursk, and U. Levy, On-chip multi spectral frequency standard replication by stabilizing a microring resonator to a molecular line, Appl. Phys. Rev. **109**, 011103 (2016).

[61] Q. Zhu, C. Qiu, Y. He, Y. Zhang, and Y. Su, Self-homodyne wavelength locking of a silicon microring resonator, Opt. Express **27**, 36625 (2019).

[62] J. Wang, K. Liu, M. W. Harrington, R. Q. Rudy, and D. J. Blumenthal, Silicon nitride stress-optic microresonator modulator for optical control applications, Opt. Express **30**, 31816 (2022).

[63] X. Lu, Q. Li, D. A. Westly, G. Moille, A. Singh, V. Anant, and K. Srinivasan, Chip-integrated visible-telecom entangled photon pair source for quantum communication, Nat. Phys. **15**, 373 (2019).

[64] A. Siddharth, W. Weng, G. Lihachev, J. Riemensberger, H. Tian, J. Liu, S. A. Bhave, and T. J. Kippenberg, Actuation bandwidth extension of an integrated piezo-optomechanical nanophotonic device, in *Conference on Lasers and Electro-Optics* (Optica Publishing Group, Washington, DC, 2021) p. STu4D.7.

[65] A. Wu, Q. Zhang, and A. W. Poon, Integrated Si_3N_4 microresonator-based quantum light sources with high brightness using a subtractive wafer-scale platform, Opt. Express **29**, 24750 (2021).

[66] W. Wen, Z. Chen, L. Lu, W. Yan, W. Xue, P. Zhang, Y. Lu, S. Zhu, and X.-S. Ma, Realizing an Entanglement-Based Multiuser Quantum Network with Integrated Photonics, Phys. Rev. Appl. **18**, 024059 (2022).